



High-order surface tension VOF-model for 3D bubble flows with high density ratio

Daniel Lörstad, Laszlo Fuchs *

Department of Heat and Power Engineering, Lund University, Ole Römers väg 1, Box 118, SE-22100 Lund, Sweden

Received 15 August 2003; received in revised form 31 March 2004; accepted 1 April 2004
Available online 7 May 2004

Abstract

An improved Volume of Fluid (VOF) method is presented which is applicable to high density ratio 3D flows for a large range of bubble Reynolds number (Re). The method is based on the Navier–Stokes equations for incompressible multi-phase flows which are discretized on a Cartesian staggered grid. The multi-grid technique together with the pressure–velocity coupling scheme for multi-phase flows have resulted in an efficient solver which nearly exponentially converge with the number of iterations. The convergence speed also shows negligible dependence on density ratio, viscosity ratio and Re . A second-order accurate, non-diffusive, mass conservative phase transport model is presented which does not suffer from unphysical over- or under-shoots of the phase variable. The high accurate normal, curvature and surface tension force model in combination with the high-order defect-correction scheme for multi-phase flows shows second-order global accuracy when applied to the transient bubble rise where the viscosity ratio is equal to one. In contrast, the commonly used viscosity model for VOF introduces a first order error for the same problem. The VOF method has been tested for different types of bubble flows at low Re and for path-oscillating and wobbling air bubbles (in water) with a diameter range of $1.82 < D < 6$ mm. The numerical results agree quantitatively with the available experimental data. The investigations show that the proposed high accurate surface tension model can be used successfully for wobbling flows with bubble deformation while maintaining the mass of the phases. The error in mass conservation is directly proportional to the residual in solving the discrete problem.

© 2004 Elsevier Inc. All rights reserved.

PACS: 61.20.Gy; 61.20.Ja; 68.03.Cd; 68.03.Kn; 68.03.Hj; 68.05.Cf

AMS: 76T10

Keywords: Volume of Fluid; Bubble two-phase flows; Surface tension; Curvature

* Corresponding author. Tel.: +46462224300; fax: +46462224300.

E-mail addresses: daniel.lorstad@vok.lth.se (D. Lörstad), laszlo.fuchs@vok.lth.se (L. Fuchs).

1. Introduction

Bubbles play an important role in many industrial applications such as bio-reactors, chemical industry, boiling and cavitating turbines, pumps and ship propellers. The motion of bubbles may be very complex. They may be subject to break-up or coalescence and may appear to move with a spiraling, zig-zagging or rocking behavior. In addition to their path-instability the bubbles may undergo large shape deformation and this oscillatory behavior of both path and shape of a bubble is often referred to as it is “wobbling”. The phenomena, which are associated with fluids of high-density ratio and low viscosity are not yet fully understood. In particular, the motion, the wake and the shape of bubbles are the subjects of active research. Both Scardovelli and Zaleski [40] and Magnaudet and Eames [25] have emphasized the importance of full 3D, non-axisymmetric computations of wobbling bubbles in order to understand the underlying physics of bubble flows.

Yet, only a limited amount of numerical work can be found in the existing literature. This is due to the different numerical difficulties related to the simulations of wobbling bubbles. One of the aims of this paper is to report a second-order, stable and numerically efficient scheme for handling bubble flows. Such a detailed investigation for wobbling bubble flows using Volume of Fluid (VOF) has so far not been found in the literature.

One may find several different methods and models for handling the flow of immiscible fluids. These approaches may be used to obtain detailed information about the motion and deformation of bubbles or droplets. The different approaches include the VOF methods [23,24,33,37], Immersed Boundary methods [24,48], Level Set methods [31,42], Moving-grid methods [3,38], Lattice–Boltzmann methods [50] and combinations of these methods [9,44]. Numerous authors have presented numerical investigations related to bubble flows. In most cases, one has focused on non-wobbling bubbles in order to study the rise velocity and/or the bubble shape [14,27,38,42,45,49,52] and the merging and/or the breakup of bubbles [5,33]. Another topic of common interest is the behavior of lift [10,19,21,28] and multiple bubble interactions [11,41,44,48]. An investigation of a path-oscillating bubble of fixed shape is presented in [29]. Most of the investigations have been restricted to bubbles where one or more of the following assumptions are applicable: (i) the flow is axisymmetric, inviscid and/or steady; (ii) the Reynolds number is low; (iii) the density ratio and/or the viscosity ratio of the fluids are not too large or small; (iv) the surface tension forces are small and (v) the deformation of the bubbles is small. Several of the above-mentioned reported numerical results lack accuracy estimates. The comparisons with experimental data have been primarily of qualitative character only. Of course, reliable numerical methods require validation by estimating the asymptotic behavior of the approach and estimating the level of accuracy for a given computation for a well-defined problem.

There are several numerical issues that must be taken into consideration when computing the motion of air bubbles in water. The high density ratio (about 1000:1) may cause slow convergence and the modeling of the surface tension force may lead to accuracy problems. Another important issue is the global mass conservation during the computations. Since the investigation of wobbling bubbles requires simulations over a long period of integration times, all schemes that do not guarantee mass conservation will, sooner or later, result in unacceptable mass losses. Level Set (LS) methods and Immersed Boundary (IB) methods may cause mass losses of the order of 1% after relatively short computational times for full 3D problems [11,41,43]. However, the difficulty with the IB method can be reduced by introducing an explicit correction for the error in mass conservation [24,48]. VOF approaches using a mass conservative scheme do not need explicit mass correction since the losses in general are small (of the order of 100 times less [33,44], related primarily to convergence or machine accuracy). Other advantages of VOF methods are that bubble break-up and coalescence are handled implicitly. The main drawback with VOF methods is usually related to the calculation of the interface curvature. Recent progress in curvature modeling seems to indicate that this issue is being resolved (cf. [24,34]). However, these curvature models have not yet been tested concerning

flows of larger Reynolds numbers and high values of density- and viscosity-ratio, which are found for wobbling air bubbles in water.

Our focus here is on the numerical issues described above and effort is made to perform a detailed, quantitative comparison with experimental data in order to evaluate the accuracy of the presented approach. We also evaluate the accuracy for particular test cases of relevance to bubble flows. Path-oscillating and wobbling air bubbles in water in the *Surface Tension Force Dominant regime* [47] has been selected for this study. The bubbles in this regime have an equivalent diameter in the range between the local maximum of the rise velocity at $D \approx 1.82$ mm [7] and the local minimum at $D \approx 6$ mm [47].

2. Governing equations

The transport of mass and momentum for an incompressible, isothermal flow of Newtonian fluids may be expressed in dimensionless form as

$$u_{j,j} = 0, \quad (1)$$

$$\rho(u_{i,t} + V_{i,t} + u_j u_{i,j}) = -p_{,i} + \frac{(\mu(u_{i,j} + u_{j,i}))_{,j}}{Re} + \frac{\rho}{Fr^2} + \frac{\kappa n_i \delta_{\text{int}}}{We}, \quad (2)$$

where u_i is the flow velocity, V_i is a uniform velocity due to the motion of the reference system, p is the pressure, ρ is the density, μ is the kinematic viscosity, $Re = \rho_0 UL / \mu_0$ is the Reynolds number, $Fr = U / \sqrt{gL}$ is the Froude number, $We = \rho_0 U^2 L / \sigma$ is the Weber number, κ is the interface curvature, n_i is the interface normal and δ_{int} is the Dirac's function which is zero except at the interface. All variables are made dimensionless using the density ρ_0 , the viscosity μ_0 , the surface tension coefficient σ , gravity g and the characteristic scales for velocity U and length L .

3. Numerical methods

The governing equations (1) and (2) are discretized on a staggered Cartesian grid system, including local mesh refinements at regions with larger gradients. The formal order of the discretization of the momentum equations of both phases is third- and fourth-order for the convective and the other terms, respectively. These equations are integrated in time using an implicit scheme. The implicit problem is solved by a multi-grid (MG) method as described below.

The pressure–velocity coupling used here is based on the simultaneous update of the dependent variables, using a SIMPLE like approach, similar to the one for single-phase flows as described in [12]. Here, however, the variable density and viscosity field are taken into account. In short, the iteration process consists of a velocity update using the residuals of the momentum equations divided by the diagonal terms combined with a simultaneous velocity and pressure update using the residual of the continuity equation. The latter is made in such a way that minimizes the change of the momentum equation residuals. Thus, the pressure correction (Δp) is computed by the following expressions:

$$\Delta p(P_{i^+,j,l} + P_{i^-,j,l} + P_{i,j^+,l} + P_{i,j^-,l} + P_{i,j,l^+} + P_{i,j,l^-}) = -h * u_{k,k}, \quad (3)$$

where

$$P_{i^+,j,l} = \left[Q_{i^+,j,l} + \frac{2\mu_{i,j,l}}{h} \left(1 + \frac{Q_{i^+,j,l}}{Q_{i^-,j,l}} \right) \right]^{-1}, \quad Q_{i^+,j,l} = \frac{3h}{2\Delta t} \rho_{i^+,j,l} + \frac{8\mu_{i^+,j,l}}{h}$$

and h is the local cell width. The indices i, j, l refer to the computational cell and the indices $+$ and $-$ specifies the cell edge, where the components of the velocity vectors are defined on the staggered grid. The simultaneous velocity correction is obtained by $\Delta u_{i^+,j,l} = P_{i^+,j,l} \Delta p$. The values of P , Q and Δu for the other cell edges are obtained using corresponding expressions. The update scheme is applied in a way that keeps flow symmetry in each Cartesian direction.

As stated above, a MG solver is used to solve the implicit problem in each time step. This solver is highly efficient and enhances considerably the convergence rate [13]. Certain modifications of the original scheme (described below) are required for handling the discontinuities in several parameters. The basics of the multi-grid procedure used here (V-cycle) can be summarized by the following steps:

- (1) Consider the system of algebraic equations that is to be solved: $A_m(a_m) = B_m$, where a is the vector of the dependent variables (u_i, p), $1 \leq m \leq M$, and where $m = 1$ is the coarsest grid level and $m = M$ is the finest one. The V-cycle is started with $m = M$.
- (2) One carries out N_m relaxation sweeps on the given grid level m . The smoothed variable a on grid m is “restricted” to the coarser grid ($m - 1$) using an averaging (interpolation) scheme, denoted by I_{m-1}^m . The same restriction operator is used both for computing $a_{m-1} = I_{m-1}^m a_m$ and for the residual defect: $B_{m-1} = I_{m-1}^m [B_m - A_m(a_m)] + A_{m-1}(a_{m-1})$.
- (3) Set $m = m - 1$ and repeat Steps 2 and 3 until $m = 1$.
- (4) Make \tilde{N}_m relaxation (smoothing) sweeps on grid level m and transfer (“prolongate”) the corrections in a from grid m to the finer one ($m + 1$) by the interpolation scheme \tilde{I}_{m+1}^m using $a_{m+1} = a_{m+1} + \tilde{I}_{m+1}^m (a_m - I_{m+1}^{m+1} a_{m+1})$.
- (5) Set $m = m + 1$ and repeat Steps 4 and 5 until $m = M$.
- (6) The MG cycle is repeated until convergence.

The I operators (I and \tilde{I}) define the data transfer (interpolation) from one level (superscript) to another level (subscript). For the prolongation step, \tilde{I} , second-order accurate Lagrangian interpolation is used for the corrections in the dependent variables, except for the boundaries of a local refinement where a fourth-order scheme is applied on the dependent variables themselves. The restriction step is a second- and fourth-order mass conserving space averaging scheme for the inner domain and at the boundaries, respectively. Thus, this averaging operator depends on the discretization scheme used for the continuity equation (1). Throughout this paper, unless otherwise specified, two V-cycles are used in each time step. In each V-cycle two simultaneous momentum/continuity sweeps (iterations) and six additional continuity relaxation sweeps are made on each grid level, except for the coarsest one where more iteration sweeps are made (until a coarse grid convergence is reached).

The presence of discontinuous fields may compromise the convergence significantly. Hence, a few issues regarding multi-phase flows have to be addressed in order to maintain the convergence rate for large density ratio cases. The density field is computed at cell edges on the finest grid level using the phase distribution (described in the following section) and is transferred to the coarser grids. The density of one edge of a coarse cell of grid ($m - 1$) is the average of the corresponding four cell edges on the finer grid (m). The viscosity field is obtained at cell centers and the value of a coarse cell on grid ($m - 1$) is the average of the corresponding eight cells belonging to the finer grid (m). In order to maintain global mass conservation in each iteration, the sum of residuals of the continuity equation on coarser grids is always corrected to yield zero (i.e., global continuity). In addition, one has to ensure that the mass fluxes through the boundaries of the locally refined grids are conserved. Without global mass conservation, the MG solver cannot converge to machine accuracy (only to a level of the order of the truncation error).

The time integration of the Navier–Stokes equations ((1) and (2)) is done by an implicit scheme using second-order accurate temporal discretization. The implicit problem is solved by using the MG approach as described above. Since the smoothing properties of higher-order schemes are less favorable as compared to lower-order schemes, we use a defect-correction approach for the momentum equations (2) that combines

the numerical accuracy of the high-order schemes with the numerical efficiency of the lower-order ones. The basic defect correction approach for solving the equation $A(a) = B$ can be written as:

$$A_{\text{low}}(a_{(i+1)}) = B - A_{\text{high}}(a_i) + A_{\text{low}}(a_i), \quad (4)$$

where A_{low} and A_{high} are the low- and higher-order discrete approximations to A . a_i is the approximation in step i during the iterative process. Obviously, if the iterative process converges, the solution is the same as solving the higher-order problem directly. The main advantages of using defect corrections are twofold: On one hand the smoothing properties of the lower-order operator are better in the MG context. Secondly, and more importantly, it can be shown [13,16] that the number of iterations in solving (2) can be limited to one or two. The level of accuracy of the result is the same as that of the truncation error, if a single step ($i = 0$, in (4)) is used, when the lower and higher order operators are of second- and fourth-orders, respectively. For time-dependent problems (as the one that is addressed here), it can be shown that a corresponding approach can be used. That is, the defect can be computed at a given time-step and is used in computing the higher order defect for the next time-step. The MG solver uses a lower-order scheme (second-order central differences for all terms in (1) and (2) except for the convective terms for which a first-order upwind scheme is used). In the higher-order scheme of (2), the second-order approximations are replaced by fourth-order (inside single phase regions), whereas the first-order is replaced by a third-order upwind scheme (everywhere).

A summary of the numerical methods used throughout this paper is presented in Table 1. A schematic form of the algorithm used here is as follows:

Given the solution for time-step $n - 1$, the following algorithm is used for time-step n :

- (1) Adjust the grid velocity V_i^n (when moving grid is used to follow the moving bubble).
- (2) Update the phase field α^n (described below).
- (3) Update density, viscosity and surface tension forces (described below).
- (4) Update the defect for high-order accuracy.
- (5) Solve for the new pressure and the velocity fields using the MG solver until the convergence condition is achieved, which completes the solution for time step n .
- (6) Set $n = n + 1$ and go to (1).

Table 1
Summary of the numerical methods

Multiphase method	Eulerian (VOF)
Grid system	Cartesian, staggered
Flow solver	Simultaneous pressure–velocity coupling
Spatial discretizations	Convection/other terms: first/second order
Defect-correction (spatial discretizations)	Single-step update of momentum equations Convection terms: third order Other terms (single-phase regions): fourth order
Temporal discretization	Second-order implicit for velocity
Multigrid	Relaxation for u , v , w and p
Interface tracking	Phase function α
Phase transport	Youngs’s model using Direction Split technique
Interface normal model	DAN model
Interface curvature model	DAC model
Surface tension model	Continuum Surface Force model (CSF)
Time marching	Explicit for α , implicit for u , v , w and p

4. Volume of Fluid

Volume of Fluid is a widely used approach for bubble transport [14,15,23,24,33,37,46]. It is based on the use of an auxiliary variable α that defines the amount of each fluid in the computational cells and where α is restricted by $0 \leq \alpha \leq 1$. Both density and viscosity can then be calculated by averaging and using the phase variable as the weight:

$$\Phi = \Phi^{(2)} + (\Phi^{(1)} - \Phi^{(2)})\tilde{\alpha}, \quad (5)$$

where the indices denote the different fluids and Φ equals to either ρ or μ . Numerically, one cannot support a discontinuity by a local polynomial approximation for the discretizations (such as with finite differences and finite elements). Therefore, the steepest gradients must be resolved on at least 2–3 computational cells (in each direction). If wider stencils are used, which is the case for higher order schemes, even larger number of cells has to be used to describe discontinuities if problems due to numerical oscillations are to be avoided. Therefore, a smoothed (averaged) phase variable $\tilde{\alpha}$ is introduced (and hence momentum is not fully conserved). This is done by employing the following cubic kernel [37]:

$$\tilde{\alpha}_{ijk} = \frac{\sum_{l,m,n} \alpha_{lmn} K(|X_{ijk} - X_{lmn}|, \gamma) dx_1 dx_2 dx_3}{\sum_{l,m,n} K(|X_{ijk} - X_{lmn}|, \gamma) dx_1 dx_2 dx_3}, \quad (6)$$

where $K(r, \gamma)$ is defined by

$$K(r, \gamma) = \begin{cases} \left(1 - 6\left(\frac{r}{\gamma}\right)^2 + 6\left(\frac{r}{\gamma}\right)^3\right) & \text{if } \frac{r}{\gamma} < \frac{1}{2}, \\ 2\left(1 - \frac{r}{\gamma}\right)^3 & \text{else if } \frac{r}{\gamma} < 1, \\ 0 & \text{otherwise,} \end{cases} \quad (7)$$

where $\gamma = 3h$ is a smoothing length-scale and h is the local cell width.

5. Surface tension modeling

Surface tension effects enter into the momentum equations (2) as a source term. In order to compute the surface tension force, one has to compute the local curvature of the bubble surface which requires the computation of the vector normal to the bubble surface. All these steps involve the computation of gradients over the bubble surface, where the dependent variables and physical parameters are discontinuities.

The surface tension forces, i.e., the last term in Eq. (2) can, according to the Continuum Surface Force (CSF) model, be expressed as

$$F_i^{\text{CSF}} = \frac{\kappa}{We} n_i \delta = \frac{\kappa}{We} \alpha_{,i}. \quad (8)$$

The CSF model has been introduced by Brackbill et al. [4]. However, the free-standing interface normal is needed for both the phase transport and the curvature estimation which are described below. Therefore, the normal is determined in all cells where $0 < \alpha < 1$ using a procedure that is referred to here as the Direction Averaged Normal (DAN) model. In the DAN model, a rough approximation of the normal is first obtained, using discretization of the α field ($n_i = \alpha_{,i}$) in the region around the computational cell under consideration (i.e., 3^3 cells). In order to improve the accuracy of the surface normal, a local coordinate system (x_1, x_2, x_3) is defined where x_3 is parallel to the largest component of the normal (v_3). The interface is

reconstructed using a distance function f which is the distance along v_3 from $x_3 = 0$ to the interface. This distance function is obtained by summation of the α field along v_3 using the following definition:

$$f(x_1, x_2, x_3) = \frac{1}{2} + N_{\text{up}} - \sum_{n=-N_{\text{low}}}^{n=N_{\text{up}}} \alpha(x_1, x_2, x_3 + nh), \quad (9)$$

where $N_{\text{up}} = N_{\text{low}} = 1$ is the number of cells in positive/negative v_3 -direction that is to be included in the summation and h is the cell width. f can be used to estimate the normal using

$$n_j(\alpha_{x_3}, f) = \frac{\alpha_{x_3}}{|\alpha_{x_3}|} (-f_{x_1}, -f_{x_2}, 1). \quad (10)$$

It is sufficient to obtain f at $(x_1, x_2) = (0, \pm h/2)$ and $(\pm h/2, 0)$ to achieve the normal. Fig. 1(a) shows a 2D example of an α -field and Fig. 1(b) shows the resulting f values which are used to reconstruct the interface by a plane as shown in Fig. 1(c). This plane corresponds to a volume fraction field (with details given in the Appendix A) that may not be identical to the original field. For example, in Fig. 1(c) the total volume fraction of the six cells within $-3h/2 < x < h/2$ and $-3h/2 < z < 3h/2$ is 5.04 which differs from the original value of 5.1. Therefore, f is corrected using the difference in the summed volume fractions. This, in turn, requires an iterative procedure until the convergence of Eq. (10) and f . The iterative procedure is stable and converges in a small number of iterations. The final result of the normal is shown in Fig. 1(d). Finally, the normal (n_1, n_2, n_3) is transformed into (n_x, n_y, n_z) . In summary, the DAN approach reduces the problem from $n(\alpha(x, y, z))$ into $n(\alpha_{x_3}, f(x_1, x_2, x_3 = 0))$. Compared to the methods of Puckett et al. [33] and Renardy and Renardy [34] who uses 3^3 (in 2D they use 3^2) cells in their minimization procedure, the DAN approach is much simpler since the number of relaxation variables is reduced to 2^2 (i.e., $f(\pm h_1/2, 0, 0)$ and $f(0, \pm h_2/2, 0)$).

The curvature $\kappa = -n_{j,j}$ is calculated using the Direction Averaged Curvature (DAC) model [23,24]. The DAC model uses the approach of summation of the α field in maximum normal direction v_3 into f in a

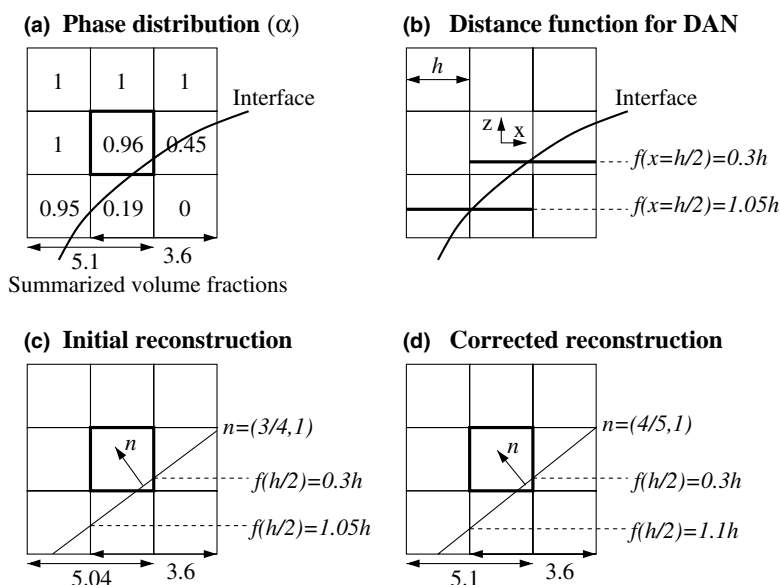


Fig. 1. Two-dimensional example of the DAN model.

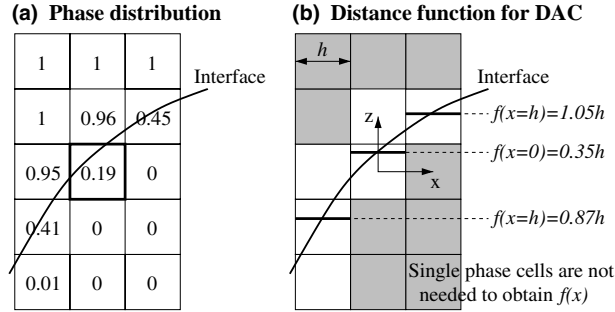


Fig. 2. Two-dimensional example of the distance function for the DAC model.

similar way as the DAN approach. However, DAC requires 3^2 values of $f(x_1, x_2, x_3 = 0)$ in order to calculate the curvature using

$$\kappa = \frac{\alpha_{,x_3}}{|\alpha_{,x_3}|} \left(\frac{f_{,jj}}{|n|} - \frac{f_{,i} f_{,j} f_{,ij}}{|n|^3} \right). \quad (11)$$

In contrast to DAN, cells that are further than one cell away in x_3 -direction may be required (i.e., outside the 3^3 cells) in the summation procedure of Eq. (9) ($N_{\text{up}} \geq 1$ and $N_{\text{low}} \geq 1$). This is needed in order to track all parts of the reconstructed interface in the region of $|x_1| \leq (3h/2)$ and $|x_2| \leq (3h/2)$, which is important in order to maintain the high accuracy of the DAC approach. A 2D example is shown in Fig. 2 where the relevant cells that are needed for DAC are shown. The cells that are required to obtain f (i.e., the interface cells) are found using the DAN model. Both the magnitude of the curvature and the location where the curvature is computed are used when computing the smoothed values of the curvature (using Eq. (7) as smoothing kernel) at the vertices of the computational cells that contain fluid of both phases. Furthermore, the curvature is computed only at computational cells for which $|f(0,0)| \leq (h/2)$. This choice can be motivated by considering the active cell of Figs. 1(a) and 2(a), i.e., the cell marked with a thick line. The results for the curvature are the same for these two active cells. One avoids repeated computation of the curvature by requiring $|f(0,0)| \leq (h/2)$ and in this way, the curvature is computed only for the active cell of Fig. 2(a).

To summarize, the DAC approach requires no iteration procedure and it has been shown to be second-order accurate by Lörst ad et al. [24]. Their investigation also show that the so-called spurious currents due to the pressure jump at the interface are very small and reduced with second-order accuracy [24]. A summary of these results is found in Lörst ad [23] together with an additional investigation which shows that the spurious currents vanish with time.

6. Phase transport

Eqs. (1) and (2) have to be complemented by the phase transport equation for α (with $0 \leq \alpha \leq 1$) in order to identify the local volume fractions of the phases. The phase transport equation expresses the conservation of one of the phases. The second phase is then conserved automatically if the continuity equation is satisfied. The phase transport equation is

$$\alpha_{,t} + (u_j \alpha)_{,j} = 0. \quad (12)$$

This equation is solved using the method of Youngs [53] combined with the direction split technique of Rudman [36]. In the direction-split method, one time step of the 3D problem is solved using three 1D problems solved one after the other, one in each direction. In order to avoid systematic errors, the order of the directions is interchanged each time step. For symmetric flow fields, the averaged phase distribution due to different direction combinations is used in order to maintain the symmetry. This results in a double number of updates for 2D symmetry and six times more for 3D symmetry.

In order to maintain mass-conservation of the phase update, vanishing divergence of the velocity vector field is required. For the direction split techniques, however, another problem arises since mass cannot be conserved until all directions are taken into consideration. Hence, α values larger than unity may arise after the first sweep which in turn may violate the restriction of $0 \leq \alpha \leq 1$ for the following sweeps. One remedy for this difficulty is by introducing the effective volume of the cells. Here, the effective volume is defined as

$$\delta V_{ijl}^k = \delta V_{ijl}^0 - \Delta t \sum_{q=1}^k \frac{\Delta u_{ijl}^q}{\Delta x_{ijl}^q}, \tag{13}$$

where $\delta V_{ijl}^0 = 1$, $1 \leq k \leq 3$ is the number of the sweep (which also defines the direction), i, j and l define the present cell, Δt is the time step, Δx_{ijl}^q is the cell size in the q -direction and Δu_{ijl}^q is the difference in velocity between cell edges in q -direction. Note that $\delta V_{ijl}^3 = 1$ since second-order central differences is used for Eq. (1). The α field is then updated using

$$\alpha_{ijl}^{n+1,k} = \frac{\alpha_{ijl}^{n+1,k-1} \delta V_{ijl}^{k-1} - \Delta F_{ijl}^k}{\delta V_{ijl}^k}, \tag{14}$$

where $\alpha_{ijl}^{n+1,0} = \alpha_{ijl}^n$, $\alpha_{ijl}^{n+1} = \alpha_{ijl}^{n+1,3}$ and ΔF_{ijl}^k is the flux difference of α in the k -direction.

Eq. (14) holds for cells with $\alpha = 1$ or $\alpha = 0$. Otherwise, due to the direction split procedure, there is a risk for small over- or under-shoots. Table 2 and Fig. 3 exemplify such cases when a cell is completely emptied (Case 1) or filled (Case 2) with one of the phases. For Case 1, if the total amount of α is fluxed out of the cell ($e = q$ in Table 2 and Fig. 3) then that cell should have $\alpha^k = 0$. The fourth column in Table 2, according to Eq. (14), shows that this is only the case when $\delta V^{k-1} = 1$, otherwise α^k will result in a positive or negative value. This would happen in the example of Fig. 3 if the y -direction starts the direction split procedure.

Table 2
Examples of over/undershoots of α , where $q \leq e$, $U_{out}^* = (\Delta t U_{out}^k)/h$ and $U_{in}^* = 0$

Case	α^{k-1}	F_{out}^k	$\alpha^k \delta V^k$: Eq. (14)	$F_{out}^{k,corr}$: Eq. (15)	$\alpha^k \delta V^k$: Eqs. (14) and (15)
1	e	q	$\delta V^{k-1} e - q$	$\delta V^{k-1} q$	$\delta V^{k-1} (e - q)$
2	$1 - e$	$U_{out}^* - q$	$1 - (\delta V^{k-1} e - q)$	$U_{out}^* - \delta V^{k-1} q$	$1 - \delta V^{k-1} (e - q)$

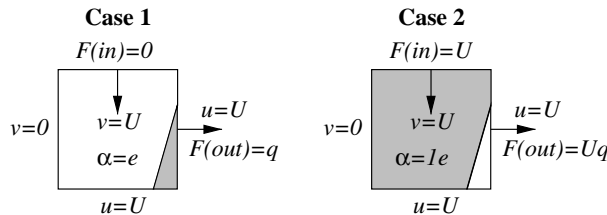


Fig. 3. Two-dimensional example of a simple flow field that may completely empty (Case 1) or fill (Case 2) a cell of α .

Then $\delta V^{k=1} > 1$ which results in $\alpha^{k=2} > 0$ and hence that cell cannot be completely emptied. The problem is similar for Case 2. Rider and Kothe [35] also have a similar problem which they solve using redistribution in order to limit α into the admissible range ($0 \leq \alpha \leq 1$) and maintain mass conservation. However, the problem of not being able to completely empty a cell or to totally fill it remains. Another way to avoid the problem is to use a flux correction scheme as shown in the last two columns of Table 2.

The fluxes cannot be corrected for filled cells without compromising the accuracy of Eq. (14). Therefore, the correction is introduced into the computation of the volume flux, that are consistent with $\alpha = 0$, i.e., $U^* - F$, where $U^* = U\Delta t/h$ and F is the flux of α . Hence, the outgoing flux in Eq. (14) is replaced by

$$F_{out}^{k,corr} = \delta V^{k-1}(F_{out}^k - U_{out}^*) + \delta V^{corr}U_{out}^*, \tag{15}$$

where δV^{corr} is between 1 and δV^{k-1} and is obtained using linear interpolation between the 4 “extreme” cases in Table 3, which results in

$$\delta V^{corr} = \delta V^{k-1} + (1 - \delta V^{k-1})\xi, \tag{16}$$

where

$$\xi = \begin{cases} \xi_1 = F_{out}^k/U_{out}^k & \text{if } |\xi_1 - \frac{1}{2}| \geq |\xi_2 - \frac{1}{2}|, \\ \xi_2 = \frac{\alpha - F_{out}^k}{1 - U_{out}^k} & \text{if } |\xi_1 - \frac{1}{2}| < |\xi_2 - \frac{1}{2}|. \end{cases} \tag{17}$$

In order to estimate the outgoing fluxes Youngs’s method is used [53]. This method is chosen due to its ability to keep the interface sharp. Youngs’s method is based upon a geometrical strategy as opposed to finite difference discretizations. A straightforward way to calculate the Youngs’s fluxes is presented below with the help of Fig. 4.

- (1) For each cell which contains the interface, i.e., where $0 < \alpha < 1$, the normal n_j is obtained using the DAN method.

Table 3
“Extreme” cases related to flux of α

Case	Meaning	Condition	δV^{corr}
1	Minimum flux out of cell	$F_{out}^k/U_{out}^k = 0$	δV^{k-1}
2	Maximum flux out of cell	$F_{out}^k/U_{out}^k = 1$	1
3	Emptying a cell	$(\alpha - F_{out}^k)/(1 - U_{out}^k) = 0$	δV^{k-1}
4	Filling a cell	$(\alpha - F_{out}^k)/(1 - U_{out}^k) = 1$	1

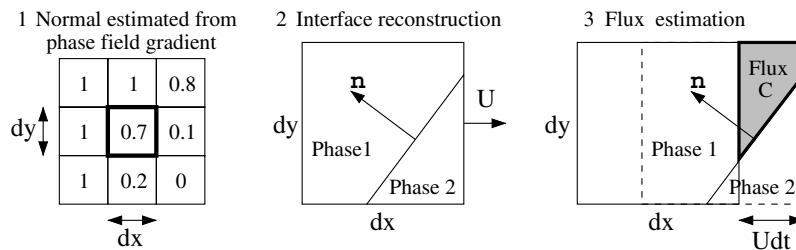


Fig. 4. Two-dimensional example of phase transport using Youngs’s model.

- (2) The interface is reconstructed using a plane $n_j x_j = d_p$, which is obtained using n_j and the volume fraction α of the present cell (see the Appendix A).
- (3) The plane is moved in the outflow direction according to $U_{\text{out}}^* = u_{\text{out}} dt/dx$.
- (4) The volume fraction C is calculated using the fluxed volume and the moved plane (see Appendix A).
- (5) The flux of α out of the cell is determined using C .

Advection tests in 3D, similar to Rudman’s 2D tests [36], have been performed where a spherical shape is placed in different analytical steady flow fields. The time-step is determined from a CFL condition of 0.2. Fig. 5(left) shows the averaged error of the entire domain, defined as $\sum(|\alpha - \alpha_{\text{exact}}|) / \sum(\alpha_{\text{exact}})$, versus cell size and time for unidirectional flow where the flow vector is $(1, 3/2, 2)$. Fig. 5(right) shows the error for a rotating flow field where the sphere is advected and deformed by the flow for a certain period of time as shown in the figure, where after it is advected back again. Hence, a perfect advection scheme would return the initial shape. The initial sphere center is placed at $(x, y, z) = (2, 2, 1)/4$, the sphere has a radius of $R = 0.2$ and the flow field is given by

$$U = \begin{cases} u = \cos(x) \sin(y) - \sin(z) \cos(x), \\ v = -\sin(x) \cos(y) + \cos(y) \sin(z), \\ w = -\sin(y) \cos(z) + \cos(z) \sin(x). \end{cases} \quad (18)$$

The figures show second-order accurate behavior in space for the unidirectional flow and for small deformations for the rotating flow whereas for the large deformations after a long period of time, the accuracy reduces slightly. In a similar manner, the error increases roughly proportional with time for both cases, however, for the rotating flow the error increases faster after some time. Fig. 6 shows the highly deformed shape at time $t = 8$ and the maximum error is in general found in the region where the gradients of the shape are high, as in the part to the far left in the figure.

The advection tests also show that the mass losses are less than $10^{-11}\%$ which confirms the mass conservative properties of the scheme (to machine accuracy) for divergence free flow fields. However, the scheme assumes zero velocity divergence $u_{j,j}$ in order to maintain mass conservation and this is, as a general rule, not the case when a phase transport model is coupled with a Navier–Stokes solver. The reason is that small residuals are often accepted since they are believed to have a small influence on the solution of the flow field. For two-phase flows, however, these residuals may act as sinks/sources of mass and integrated

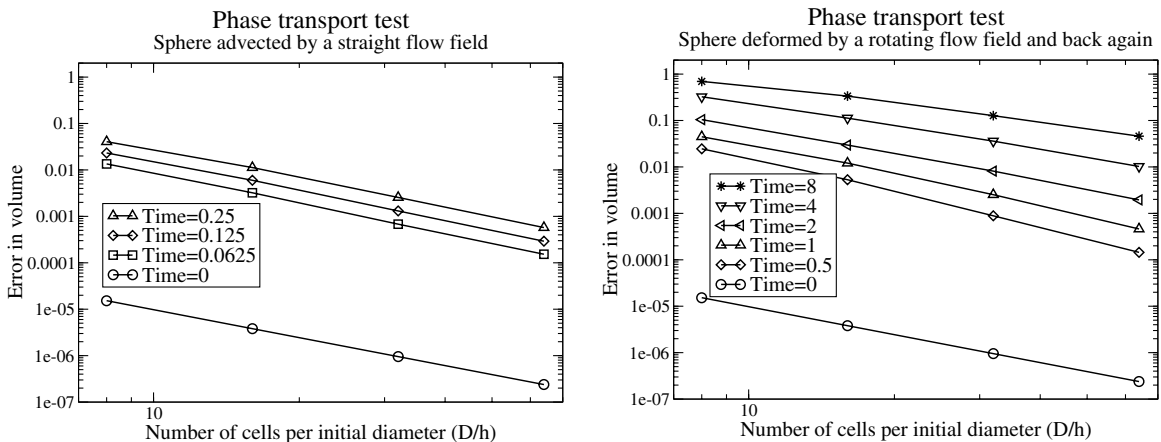


Fig. 5. Error in phase transport versus grid size and time for analytical flow fields.

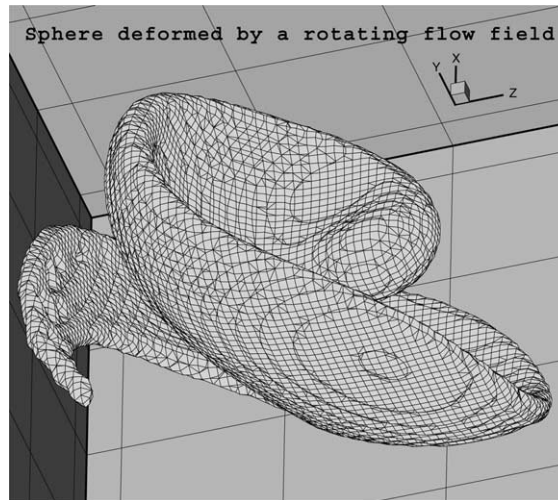


Fig. 6. A deformed sphere in a rotating flow field at $t = 8$ ($D/h = 64$).

over time they may become the most significant error and limit the time for which a computation is reasonably accurate. Therefore, it is important that a numerical scheme enables integration of multi-phase flows during a long period of time.

7. Results

First, we consider some cases concerning bubbles that have modest density jumps relative to the surrounding liquid. The Reynolds number (Re) is also relatively low. These cases are used to investigate the accuracy of the method. Further results include the computations of 3D high Re air bubbles in water and the results are compared with corresponding results in the literature.

7.1. Stokes flow

The Stokes flow ($Re = 10^{-6}$) past a fixed liquid sphere has been considered first. The density ratio $\rho_{\text{outer}}/\rho_{\text{bubble}}$ is equal to 2 and the viscosity ratio $\mu_{\text{outer}}/\mu_{\text{bubble}}$ is either 1, 2 or 10. The fixed sphere (no phase transport is used) is placed in the middle of a cube of sides equal to 2 diameters and the analytical solution [32] is defined on the boundaries. Table 4 shows the order of accuracy of the L_2 - and L_1 -norm of the error of the flow field and the bubble velocity. The bubble velocity is obtained using summation over all cells:

Table 4
Order of accuracy for the flow around a fixed liquid sphere ($Re = 10^{-6}$)

Grids		$\mu_1/\mu_2 = 1$			$\mu_1/\mu_2 = 2$			$\mu_1/\mu_2 = 10$		
		L_2	L_1	W_b	L_2	L_1	W_b	L_2	L_1	W_b
8	16	1.9	1.9	1.8	1.6	1.6	1.6	1.0	1.2	1.5
16	32	2.0	2.0	1.9	1.5	1.6	1.6	0.8	1.1	1.5
32	64	2.0	2.0	2.0	1.3	1.4	1.5	0.9	1.0	1.4
64	128	2.0	2.0	2.0	1.2	1.2	1.3	0.9	1.0	1.2

$$W_b = \frac{\sum w(1 - \alpha)}{\sum (1 - \alpha)}, \tag{19}$$

where $\alpha = 0$ defines the bubble region. The order of accuracy n is obtained by computing

$$L_{\text{solution}} = L_{\text{analytical}} + Ch^n \tag{20}$$

for different grids where C is assumed to be a constant. The results indicate that the solution is second-order accurate when the viscosity ratio is equal to unity. However, the viscosity model of Eq. (5) seems to introduce a first-order error of the solution. The underlying reason for this can be understood from the following example. Consider the flow past a flat fluid–fluid interface where the velocity profile is linear. The shear-stress is then constant and there is a velocity discontinuity at the surface according to $\tau_{xy} = \mu^{(1)}u_{x,y}^{(1)} = \mu^{(2)}u_{x,y}^{(2)}$ where the flow is in x -direction and the surface normal is in the y -direction. The indices (1) and (2) represent the two different fluids. In addition, consider three cells in y -direction across the interface such that $\alpha_{j-1} = 0$, $\alpha_j = \beta$ and $\alpha_{j+1} = 1$ where the interface position is defined by β . The analytical velocity difference equals then

$$u_{j+1} - u_{j-1} = \tau_{xy}h \left(\frac{1/2 + \beta}{\mu^{(1)}} + \frac{3/2 - \beta}{\mu^{(2)}} \right).$$

The corresponding discretization results in

$$u_{j+1} - u_{j-1} = \tau_{xy}h \left(\frac{1}{\mu_{j+1/2}} + \frac{1}{\mu_{j-1/2}} \right).$$

When the viscosity model of Eq. (5) is applied, the result is a first-order error in the velocity difference. Hence, an improved viscosity model is required in order to achieve second-order accuracy in 3D.

Furthermore, the investigation presented in Table 4 shows that the bubble velocity seems to be an appropriate measure of the order of accuracy, even though it seems to introduce an additional second-order error since the order is slightly larger than the L_2 - and L_1 -norm (defined as $L_p = \{\sum_{n=1}^N |u_n^{\text{solution}} - u_n^{\text{exact}}|^p / N\}^{1/p}$) when the viscosity ratio is different from unity. This measure will be used for the accuracy assessments in the following bubble computations where the analytical flow field is unknown.

7.2. Rising bubble at modest Re and density ratio

The next test case concerns the rise of a bubble at modest Re and density ratio as defined in Table 5. The initially spherical bubble is placed in a large domain in a zero velocity field and it is tracked as it accelerates due to gravity. All variables are made dimensionless using the equivalent diameter D (defined from: Bubble volume = $\pi D^3/6$), the reference velocity $U = \sqrt{gD}$ and the time scale $\tau = D/U$. A grid that follows the bubble and a sequence of locally refined grids around the bubble are used as depicted in Fig. 7. No-slip condition is used on all boundaries, where the no-slip boundary velocity is defined from the moving reference system (see Eq. (2)).

Table 5
Computational cases for a rising light bubble at low Re

Case	ρ_1/ρ_2	μ_1/μ_2	Re	Fr	We
1	2	1	10	1	∞
2	2	2	10	1	∞
3	2	1	10	1	40

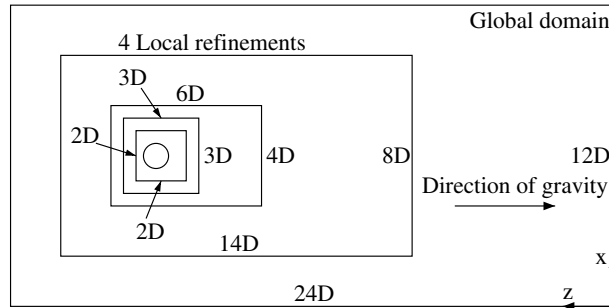


Fig. 7. The arrangement of the computational domain with locally refined grids. Each level is refined by a factor 2 in each direction.

The bubble motion is computed using different grid sizes of $6 \leq D/h \leq 64$ and the time step equals $0.32h$, where h is the cell size. Fig. 8(left) shows the bubble velocity versus time for the different bubbles. It shows that the bubble velocity is similar for the different cases and that the time gradients are small at $t = 10$ dimensionless time units. Fig. 8(right) shows the bubble velocity versus grid refinement at $t = 10$. It shows a smooth grid convergence as the grid is refined and the order of accuracy is presented in Table 6. The bubble

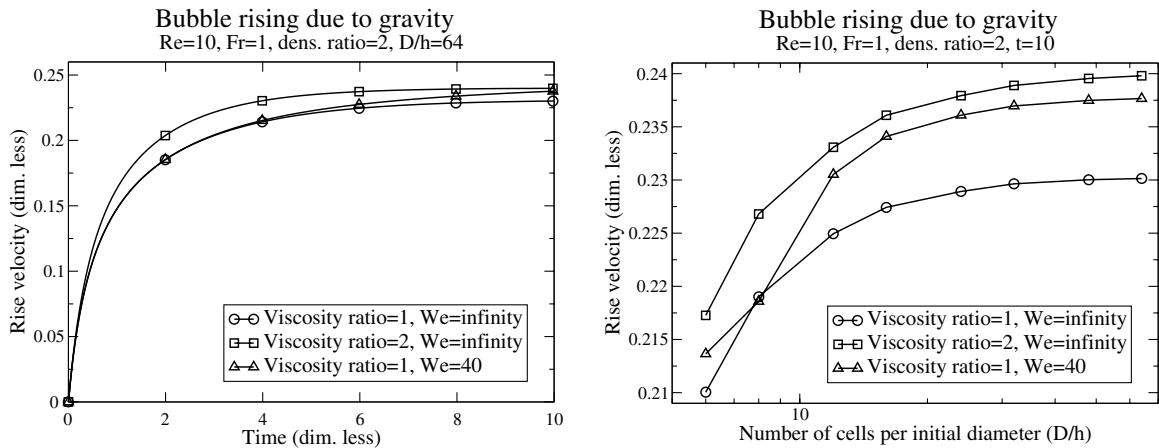


Fig. 8. Bubble velocity versus time (left) and grid size (right).

Table 6
Order of accuracy, n , for different parameter values ($Re = 10$, $Fr = 1$ and $(\rho_1/\rho_2) = 2$)

Case	1	2	3
We	∞	∞	40
μ_1/μ_2	1	2	1
Grids (D/h)	n		
24	12	6	1.9
32	16	8	1.7
48	24	12	1.6
64	32	16	1.6

velocity is obtained using Eq. (19) and the order of accuracy corresponding to the results of three different grids is obtained using Eq. (20). Table 6 shows that for a free moving bubble, including surface tension and modest values of Re and density ratio, the bubble velocity shows a second-order accurate behavior. However, a viscosity ratio different from unity results in a reduced accuracy which is in agreement with the Stokes flow case. Fig. 9 shows the resulting shapes and flow fields which in turn show that the bubble of lowest bubble viscosity and with no surface tension effect (Fig. 9b) is subject to the largest deformation. In addition, both bubbles of $We = \infty$ slowly deform since there are no surface tension forces to prevent it. This explains the normal velocity at the rear stagnation point, since the wake effect is about to break into the bubble and later on may cause a bubble torus. Hence, they are not close to a steady state, in contrast to the small gradients of Fig. 8(left).

7.3. Ellipsoidal air bubbles in water

The final test case concerns the full 3D computation of air bubbles moving in water. Effort is made to perform a detailed, quantitative comparison with experimental data in order to assess the accuracy of the presented approach. Extensive grid refinement studies are carried out and comparisons to several references

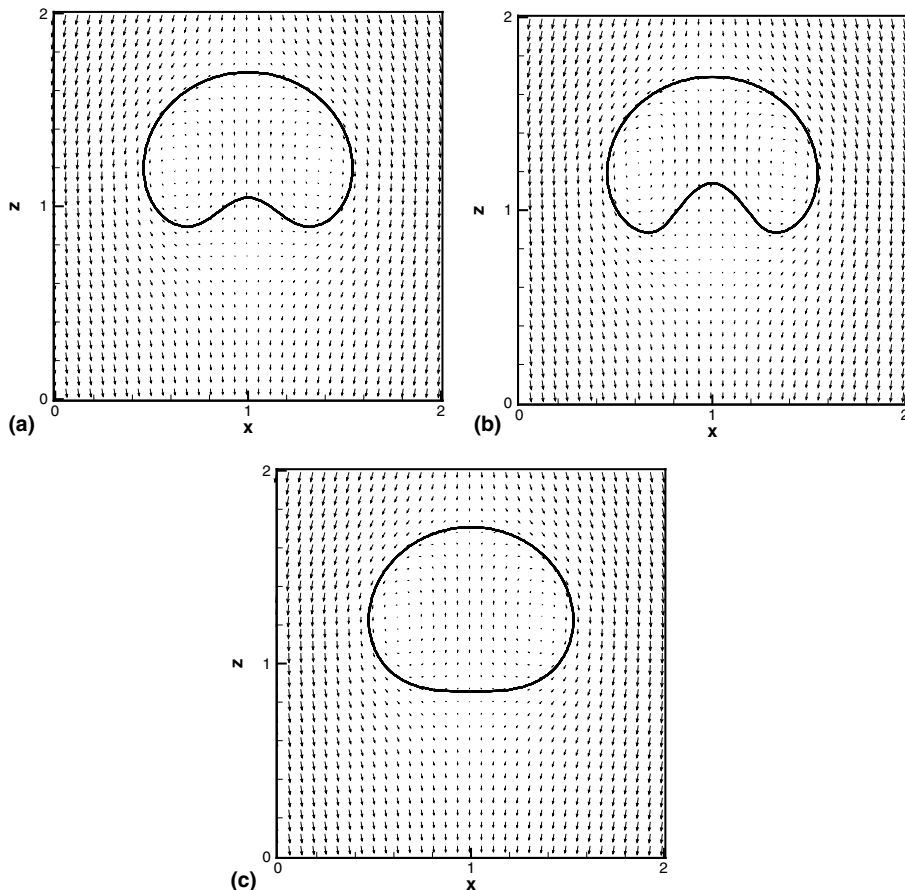


Fig. 9. The flow field and bubble shape for $D/h = 64$ at $t = 10$ for a rising bubble at $Re = 10$, where a, b and c correspond to case 1, 2 and 3 in Table 5.

for different bubble sizes and quantities are made. The comparisons include both transient and steady results. There is a rather extensive amount of literature concerning experimental investigations of single air bubbles in quiescent water rising due to gravity in a large domain [1,2,6–8,18,17,20,22,47]. The quality of the water used in the experiments is a critical issue (especially for small bubbles) [26,51,54]. Another important factor is the bubble release technique [47]. These factors are assumed to be the main reasons for the large scatter in the experimental data.

The calculations have been performed using the same grid structure and initial/boundary conditions as in the previous section (see Fig. 7). The fluid properties of water and air for density, viscosity and surface tension coefficient are as follows: $\rho_{\text{water}} = 998$, $\rho_{\text{air}} = 1.2 \text{ kg/m}^3$, $\mu_{\text{water}} = 1.003 \times 10^{-3}$, $\mu_{\text{air}} = 1.8 \times 10^{-5} \text{ kg/(m s)}$ and $\sigma = 0.0728 \text{ kg/s}^2$. All scales are made dimensionless using the fluid properties as well as D , U and τ as defined in Table 7. Four bubble sizes in the ellipsoidal region [6] are chosen in the range of $1.82 \leq D \leq 6 \text{ mm}$. By making this choice one includes the full transition region between the stable, rectilinear, axisymmetric bubble rise of $D \leq 1.82 \text{ mm}$ [7] and the unstable, oscillatory 3D motion of the larger bubbles. The grid size range is $16 \leq D/h \leq 48$ and the time step is equal to $0.08h$. The computations have been continued for at least 100 dimensionless time units for all bubble sizes for $D/h \leq 32$. Thus, we can assess the long time flow statistics for the wobbling bubbles. Additional computations using $D/h = 48$ have been performed for those bubble sizes where the asymptotic behavior indicated that the coarse grid results have to be re-computed using a finer grid. The errors due to the size of the time-step and convergence criteria are also investigated and confirmed to be very small when compared with the errors resulting from the spatial resolution (i.e. the grid size).

In order to control the break down of the axisymmetric motion into a 3D motion, an initial disturbance is added as a body force orthogonal to the gravity direction. This disturbance is decreased linearly with time until the disturbance vanishes at time $t = 1$ dimensionless unit. The magnitude of the initial disturbance in the x -direction is one-tenth of the magnitude of the gravity and half of that quantity in the y -direction. Fig. 10 shows the bubble z -velocity versus position for $D = 4 \text{ mm}$ and different grid sizes with and without the initial disturbance. The symbols from the calculations are placed one time unit apart. Comparison with the experimental data of Aybers and Tapucu [1] shows good agreement for the initial stage of the bubble rise, even though the experiments have been performed on 4.18 mm bubbles in contaminated water of $T \approx 28^\circ \text{ C}$. The transient behavior of the bubble velocity is very different after some time ($t > 6$ or $z/D > 6$) when comparing the results with or without the initial disturbance as shown in Fig. 10. The bubble behavior for different types of initial disturbances is an interesting topic since it may help to understand the physics that would explain why the motion of the bubbles are so highly sensitive to small perturbations [18,47]. These issues are, however, beyond the scope of this work.

Without any initial disturbances, the bubbles remain axis-symmetrical until about $t = 8$. Thereafter, the bubble shape loses its symmetry and becomes fully 3D for $t > 8$, as is noted in Fig. 11(left). The figure shows how the x -velocity of the bubble grow from round-off accuracy and that more iterations per time step have small influence on the speed the bubble loses its axis-symmetry. However, the breakdown of symmetry is grid-dependent, hence, it makes no physical sense to study that without a well-defined disturbance that has a significantly stronger effect than the grid.

Table 7
Computational cases for air bubbles in water rising due to gravity

Case	D (mm)	U (m/s)	τ (ms)	Re	Fr	We
1	1.82	0.36	5.06	652	0.98	4.66
2	2.5	0.309	8.09	769	1.20	3.08
3	4	0.237	16.9	942	1.97	3.27
4	6	0.238	25.2	1421	2.69	3.23

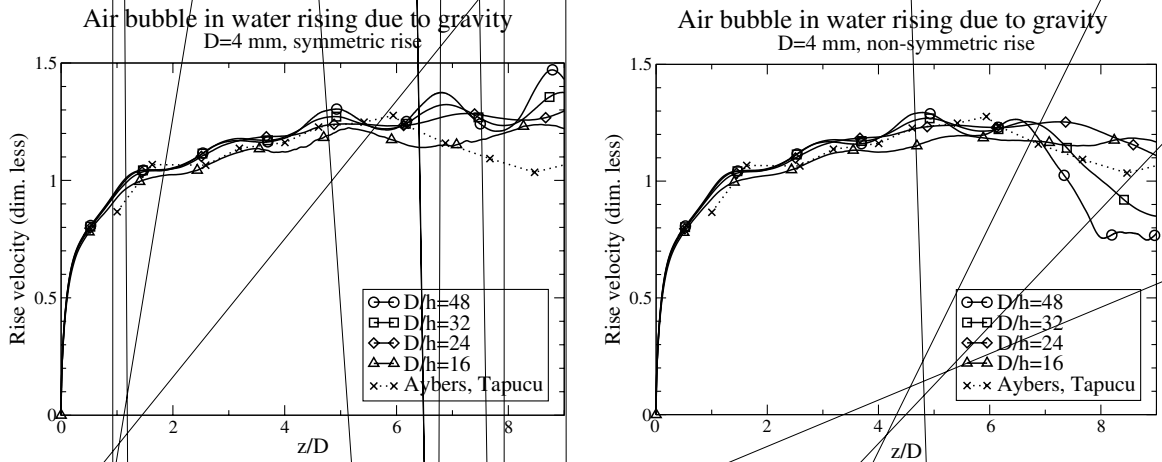


Fig. 10. Bubble velocity versus time for an air bubble in water rising due to gravity [1] with (left) and without (right) initial disturbances.

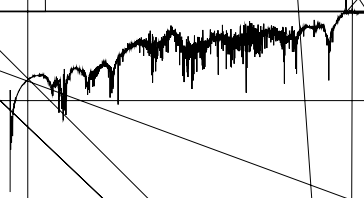


Fig. 11(right) shows the shape of the bubble and the flow field at time $t = 8$. The α contour is shown for different values in order to show that the phase transport scheme keeps the interface sharp and does not result in unphysical spots of α inside or outside the bubble. This indicates also that the phase transport scheme does not suffer from excessive numerical diffusion.

Fig. 12(left) shows the error in mass versus time for different number of V-cycles per time step. The results show that the losses in mass decrease exponentially with the number of iterations. Fig. 12(right) shows how the velocity corrections decrease with the number of V-cycles both for an air bubble and for the modest Re case (Case 3 in Table 5). The corrections are defined as the maximum correction in w -velocity

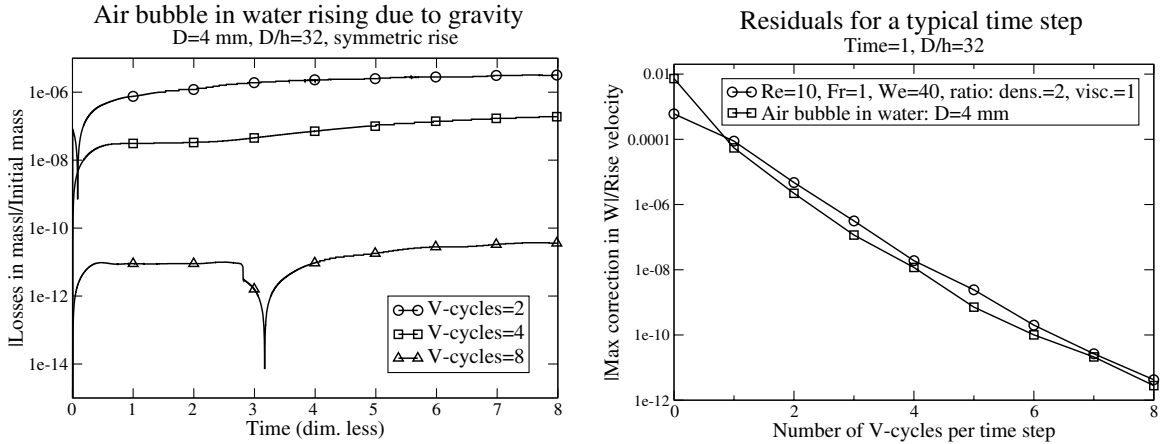


Fig. 12. Numerical accuracy: Left: Error in mass versus time for different number of V-cycles per time step. Right: Residuals versus number of V-cycles per time step.

within a multi-grid V-cycle during one time step divided by the bubble velocity. Time $t = 1$ dimensionless time unit is chosen since both cases are in the acceleration phase at that time. The reason for the exponential behavior is that the error in mass is mainly due to the residuals of the continuity equation. These residuals are composed mainly of high-frequency error components which are eliminated exponentially with the number of iterations as shown in Fig. 12(right). The results also indicate that the convergence properties of the current method are insensitive to density-ratio, viscosity-ratio or Re . In comparison, Rudman [37] needed a computational time which was approximately twice as long for density ratios of 1000 as opposed to small density ratios. Furthermore, when using only two V-cycles, the mass losses are less than 0.001% which is significantly below the losses of about 0.01% reported for other VOF approaches [33,44].

Fig. 13 shows the bubble velocity in the rise direction (left) and the velocity magnitude (right) versus the equivalent diameter for different grid sizes for both numerical results and experimental data. The results show that the bubble of $D = 1.82$ mm (which reaches a steady state) requires finer grids in order to obtain a

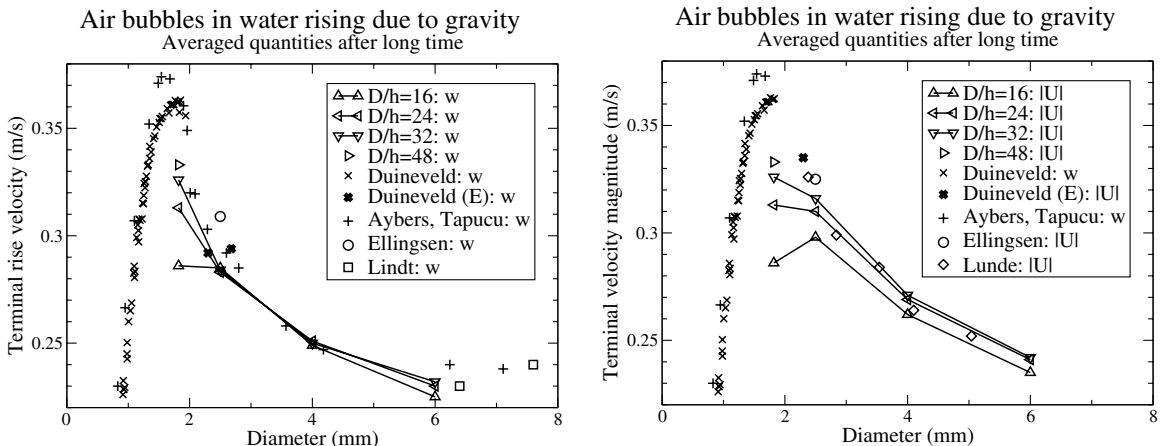


Fig. 13. Terminal velocity (left) and velocity magnitude (right) for rising air bubbles in water [2,7,8,20,22].

solution with reasonable accuracy due to the significant refinement dependency. This is not surprising since Re is high (see Table 7) and hence finer grids are needed to resolve the boundary layer of the bubble compared to the previous cases of $Re \leq 10$. The diameter of $D = 1.82$ mm is the limit between the axisymmetric rise of smaller bubbles and fully 3D rise of larger bubbles [7]. For the larger oscillatory bubbles the grid dependence is smaller despite the larger Re . Hence, the importance of resolving the bubble boundary layer seems to be less for those, at least for integrated properties such as the bubble velocity, and coarse grids may be sufficient to compute the basic physics for bubbles well inside the oscillatory (wobbling) region. We also note that the secondary motion (drift and wobbling) is more sensitive to spatial resolution than the bubble z -velocity. For the same reason the velocity magnitude requires finer grids in order to obtain a small grid dependence. All numerical results as well as the asymptotic behavior for $D = 1.82$ mm seem to be within the range of the scatter of the experimental data. In addition, the shape oscillation of the bubble of $D = 2.5$ is negligible while it is significant for the larger bubbles of $D = 4$ and 6 mm. This is also in agreement with the experimental results.

Fig. 14 show instantaneous shapes of a wobbling air bubble of $D = 4$ mm rising in water due to gravity. The figure clearly shows the un-symmetric bubble shape due to the wobbling deformation. Fig. 15(left) shows the velocity development where it is shown that the wobbling spiraling behavior is obtained fast and that the development of the transverse velocity components (u and v) differ due to the different disturbance amplitudes in x - and y -directions.

Fig. 15(right) shows the dominating path-oscillating frequency versus the diameter. The frequency content of the rise velocity is used in this figure. This frequency is approximately twice as large as the frequency corresponding to the velocities in the transversal directions. The scatter in the experimental data is large and the numerical results seem reasonable when compared to those data. Saffman [39] also measured the frequency of bubbles and obtained corresponding frequencies of around 14 Hz for zig-zagging bubbles and 10 Hz for spiral motion which agree well to our results. There are no results for coarse grids for $D = 2.5$ mm since the initial path-oscillation is damped and the final motion results in a non-wobbling and uniform velocity.

In order to investigate the mass losses after a long period of time, the relative mass losses for the bubble of $D = 4$ mm are presented here: 8×10^{-6} , 4×10^{-5} and 8×10^{-5} at time equal to 8, 50 and 100 units,

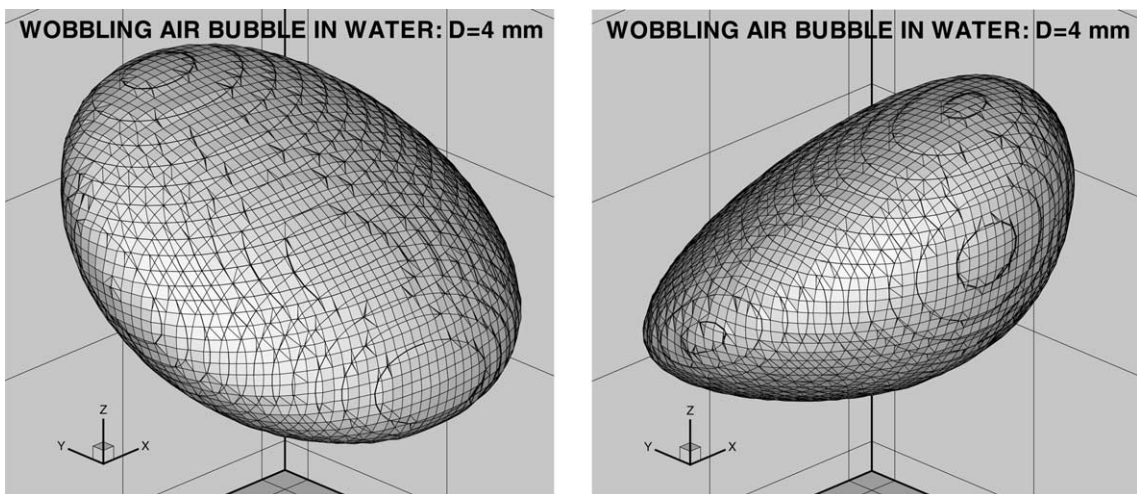
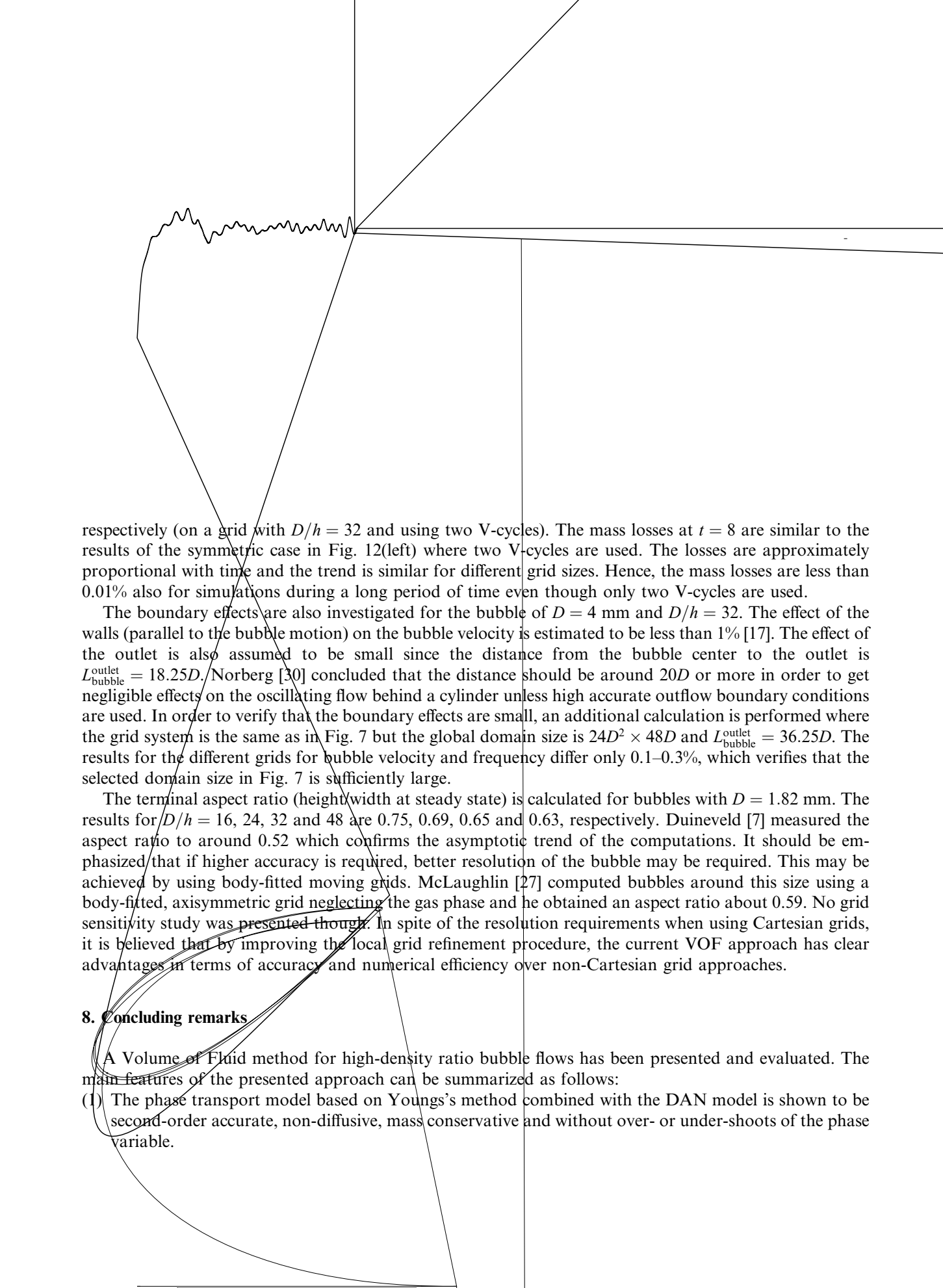


Fig. 14. Instantaneous shapes of a wobbling air bubble of $D = 4$ mm for $D/h = 32$ at $t = 100$ (left) and $t = 105$ (right).



respectively (on a grid with $D/h = 32$ and using two V-cycles). The mass losses at $t = 8$ are similar to the results of the symmetric case in Fig. 12(left) where two V-cycles are used. The losses are approximately proportional with time and the trend is similar for different grid sizes. Hence, the mass losses are less than 0.01% also for simulations during a long period of time even though only two V-cycles are used.

The boundary effects are also investigated for the bubble of $D = 4$ mm and $D/h = 32$. The effect of the walls (parallel to the bubble motion) on the bubble velocity is estimated to be less than 1% [17]. The effect of the outlet is also assumed to be small since the distance from the bubble center to the outlet is $L_{\text{bubble}}^{\text{outlet}} = 18.25D$. Norberg [30] concluded that the distance should be around $20D$ or more in order to get negligible effects on the oscillating flow behind a cylinder unless high accurate outflow boundary conditions are used. In order to verify that the boundary effects are small, an additional calculation is performed where the grid system is the same as in Fig. 7 but the global domain size is $24D^2 \times 48D$ and $L_{\text{bubble}}^{\text{outlet}} = 36.25D$. The results for the different grids for bubble velocity and frequency differ only 0.1–0.3%, which verifies that the selected domain size in Fig. 7 is sufficiently large.

The terminal aspect ratio (height/width at steady state) is calculated for bubbles with $D = 1.82$ mm. The results for $D/h = 16, 24, 32$ and 48 are 0.75, 0.69, 0.65 and 0.63, respectively. Duineveld [7] measured the aspect ratio to around 0.52 which confirms the asymptotic trend of the computations. It should be emphasized that if higher accuracy is required, better resolution of the bubble may be required. This may be achieved by using body-fitted moving grids. McLaughlin [27] computed bubbles around this size using a body-fitted, axisymmetric grid neglecting the gas phase and he obtained an aspect ratio about 0.59. No grid sensitivity study was presented though. In spite of the resolution requirements when using Cartesian grids, it is believed that by improving the local grid refinement procedure, the current VOF approach has clear advantages in terms of accuracy and numerical efficiency over non-Cartesian grid approaches.

8. Concluding remarks

A Volume of Fluid method for high-density ratio bubble flows has been presented and evaluated. The main features of the presented approach can be summarized as follows:

- (1) The phase transport model based on Young's method combined with the DAN model is shown to be second-order accurate, non-diffusive, mass conservative and without over- or under-shoots of the phase variable.

- (2) The discretization scheme including the high-accurate and highly efficient defect-correction scheme shows a global second-order accurate behavior when applied to bubble flow of modest Re and density ratio. In contrast, the results obtained using the viscosity model which is commonly used with VOF is only first-order accurate.
- (3) The multi-phase flow solver is shown to be efficient and to converge exponentially with the number of iterations. In addition, the convergence rate is not sensitive to large values in density ratio, viscosity ratio or Re .
- (4) The mass losses are shown to be very small, proportional to the residuals in the continuity equation and can be reduced to machine accuracy. No other VOF method has been reported to result in comparable values with respect to this topic.
- (5) The high accurate surface tension model which is based on the DAC model has been used successfully for wobbling air bubbles in water at high Re . Previous investigations using high accurate surface tension models for VOF [24,34] have only considered low values of density ratio, viscosity ratio and/or Re . Thus, one of the main issues in using VOF; namely, the difficulty of accurate surface tension force modeling is now remedied.

Hence, the presented VOF method is superior when high density ratio, surface tension and mass conservation are important factors, which is the case for wobbling bubbles.

We have computed bubbles at low Re as well as wobbling air bubbles in water at higher Re . Extensive grid convergence studies have been performed and the results show reasonable (quantitative) agreement with experimental data. The air bubble computations included bubbles in the range of equivalent diameters of $1.82 \leq D \leq 6$ mm. In these cases an initial disturbance has been added in order to trigger a 3D oscillatory motion. The results indicate that the resolution of $D/h = 32$ is sufficient for the larger bubbles ($3 < D < 6$ mm) for computing the basic features of the flow, such as bubble shape oscillations, wake dynamics and path-instabilities. Finer grids are recommended when studying bubbles in the transition range (bifurcation) between rectilinear and wobbling bubble rise ($1.5 < D < 3$ mm).

Acknowledgements

This work was partially supported by ELFORSK (within the program Vattenturbinteknik) and by the Swedish National Energy Administration (STEM). The authors highly acknowledge the interesting discussions and the support of Prof. Wei Shyy at the Department of Mechanical and Aerospace Engineering, University of Florida.

Appendix A. Volume fraction calculation

Here, we present a way to calculate the volume fractions of a cube which is cut into two parts by a plane. We also discuss how to obtain the plane equation $n_j x_j = d$ using a normal and a volume fraction.

First, the plane equation is sought. The difficulty is greatly reduced if the cell is scaled into a unity cube, the plane scaled similarly and the corresponding normals sorted according to

$$\begin{cases} n_1 = \max(|n_x|, |n_y|, |n_z|), \\ n_3 = \min(|n_x|, |n_y|, |n_z|), \\ n_2 = |n_x| + |n_y| + |n_z| - n_1 - n_3. \end{cases} \quad (\text{A.1})$$

These relations lead to $n_1 \geq n_2 \geq n_3 \geq 0$. The distance to the plane which involves the corner q is d_q defined from corner $q = 1$ which is the corner furthest away from the plane in the normal direction, i.e., inside the

region of $\alpha = 1$. The corresponding volume of the sliced cube between the plane and the corner number 1 is V_q . d_q and V_q are defined as

$$\left\{ \begin{array}{ll} d_1 = 0, & V_1 = 0, \\ d_2 = n_3, & V_2 = n_3^2 / (6n_1n_2), \\ d_3 = n_2, & V_3 = (3n_2^2 - 3n_2n_3 + n_3^2) / (6n_1n_2), \\ d_4 = \min(n_1, n_2 + n_3), & V_4 = \frac{2d_4 - n_2 - n_3}{2n_1} + \frac{\max(0, n_2 + n_3 - d_4)^3}{6n_1n_2n_3}, \\ d_5 = d_8 - d_4, & V_5 = 1 - V_4, \\ d_6 = d_8 - d_3, & V_6 = 1 - V_3, \\ d_7 = d_8 - d_3, & V_6 = 1 - V_3, \\ d_8 = n_1 + n_2 + n_3, & V_8 = 1. \end{array} \right. \quad (\text{A.2})$$

Due to the symmetric behavior of Eq. (A.2), the symmetric volume fraction is introduced: $\alpha_s = \min(\alpha, 1 - \alpha)$. The corresponding distance between corner number 1 and the plane can be calculated by the following interpolation:

$$d_s = \left\{ \begin{array}{ll} (6\alpha_s n_1 n_2 n_3)^{1/3} & \text{if } \alpha_s < V_2, \\ \frac{1}{2}n_3 + \sqrt{2n_1 n_2 \alpha_s - \frac{n_3^2}{12}} & \text{else if } \alpha_s < V_3, \\ \text{Solve } f_3(d_s) = 0 & \text{else if } \alpha_s < V_4, \\ \text{Solve } f_4(d_s) = 0 & \text{else if } n_1 < n_2 + n_3, \\ d_4 + (d_5 - d_4) \frac{\alpha_s - V_4}{1 - 2V_4} & \text{otherwise,} \end{array} \right. \quad (\text{A.3})$$

where

$$\begin{aligned} f_3(d) &= \frac{-d^3}{3} + (n_2 + n_3)d^2 - (n_2^2 + n_3^2)d - 2\alpha_s + \frac{n_2^3 + n_3^3}{3}, \\ f_4(d) &= \frac{-d^3}{3} + (n_1 + n_2 + n_3)d^2 - (n_1^2 + n_2^2 + n_3^2)d - 2\alpha_s + \frac{n_1^3 + n_2^3 + n_3^3}{3}, \end{aligned} \quad (\text{A.4})$$

The distance d from corner $q = 1$ may then be obtained using

$$d = \left\{ \begin{array}{ll} d_s & \text{if } \alpha \leq \frac{1}{2}, \\ d_8 - d_s & \text{otherwise.} \end{array} \right. \quad (\text{A.5})$$

Finally, the resulting plane $n_1x + n_2y + n_3z = d$ can be transformed into $n_x x + n_y y + n_z z = n_j x_j = d_p$, where (n_x, n_y, n_z) is the original normal vector and $d_p = d_m - d$ is the distance between the plane and the cell corner of minimum x , y and z where

$$d_m = \max(0, n_x, n_y, n_z, n_x + n_y, n_x + n_z, n_y + n_z, n_x + n_y + n_z). \quad (\text{A.6})$$

Next, seek the volume fraction α of a cube which is cut by a known plane. α is obtained using the symmetric volume fraction α_s by

$$\alpha_s = p \left\{ \begin{array}{ll} d^3 & \text{if } d < d_2, \\ n_3(n_3^2 - 3n_3d + 3d^2) & \text{else if } d < d_3, \\ n_2^3 + n_3^3 - 3(n_2^2 + n_3^2)d + 3(n_2 + n_3)d^2 - d^3 & \text{else if } d < d_4, \\ \sum n_i^3 - 3(\sum n_i^2)d + 3(\sum n_i)d^2 - 2d^3 & \text{else if } n_1 < n_2 + n_3, \\ \left(V_4 + (1 - 2V_4) \frac{d - d_4}{d_5 - d_4} \right) / p & \text{otherwise,} \end{array} \right. \quad (\text{A.7})$$

$$\alpha = \begin{cases} \alpha_s & \text{if } d \leq (d_8/2), \\ 1 - \alpha_s & \text{otherwise,} \end{cases} \quad (\text{A.8})$$

where $d = \min(d_m - d_p, d_8 - d_m + d_p)$ and $p = 1/6n_1n_2n_3$.

References

- [1] N.M. Aybers, A. Tapucu, The motion of gas bubbles rising through stagnant liquid, *Wärme Stoffübertrag.* 2 (1969) 118–128.
- [2] N.M. Aybers, A. Tapucu, Studies on the drag and shape of gas bubbles rising through a stagnant fluid, *Wärme Stoffübertrag.* 2 (1969) 171–177.
- [3] L.A. Bozzi, J.Q. Feng, T.C. Scott, A.J. Pearlstein, Steady axisymmetric motion of deformable drops falling or rising through a homogeneous fluid in a tube at intermediate Reynolds number, *J. Fluid Mech.* 336 (1997) 1–32.
- [4] J.U. Brackbill, D.B. Kothe, C. Zemach, A continuum method for modeling surface tension, *J. Comput. Phys.* 100 (1992) 335–354.
- [5] L. Chen, S.V. Garimella, J.A. Reizes, E. Leonardi, The development of a bubble rising in a viscous liquid, *J. Fluid Mech.* 387 (1999) 61–96.
- [6] R. Clift, J.R. Grace, M.E. Weber, *Bubbles, Drops and Particles*, Academic Press, New York, 1978.
- [7] P.C. Duineveld, The rise velocity and shape of bubbles in pure water at high Reynolds number, *J. Fluid Mech.* 292 (1995) 325–332.
- [8] K. Ellingsen, F. Risso, On the rise of an ellipsoidal bubble in water: oscillatory paths and liquid-induced velocity, *J. Fluid Mech.* 440 (2001) 235–268.
- [9] D. Enright, R. Fedkiw, J. Ferziger, I. Mitchell, A hybrid particle level set method for improved interface capturing, *J. Comput. Phys.* 183 (2002) 83–116.
- [10] E.A. Ervin, G. Tryggvason, The rise of bubbles in a vertical shear flow, *J. Fluid Engrg.* 119 (1997) 443–449.
- [11] A. Esmaeeli, G. Tryggvason, Direct numerical simulations of bubbly flows part 2. Moderate Reynolds number arrays, *J. Fluid Mech.* 385 (1999) 325–358.
- [12] L. Fuchs, H.-S. Zhao, Solution of three-dimensional viscous incompressible flows by a multi-grid method, *Int. J. Numer. Methods Fluids* 4 (1984) 539–555.
- [13] L. Fuchs, Defect-correction and higher numerical accuracy, in: W. Hackbusch (Ed.), *Proceedings of the GAMM-seminar on “Efficient Solutions of Elliptic Systems, Kiel, 1984*, pp. 55–62.
- [14] I. Ginzburg, G. Wittum, Two-phase flows on interface refined grids modeled with VOF, staggered finite volumes, and spline interpolants, *J. Comput. Phys.* 166 (2001) 302–335.
- [15] D. Gueyffier, J. Li, A. Nadim, R. Scardovelli, S. Zaleski, Volume-of-Fluid interface tracking with smoothed surface stress methods for three-dimensional flows, *J. Comput. Phys.* 152 (1999) 423–456.
- [16] J. Gullbrandt, X.S. Bai, L. Fuchs, High order Cartesian grid method for calculation of incompressible turbulent flow, *Int. J. Numer. Methods Fluids* 36 (2001) 687–709.
- [17] T.Z. Harmaty, Velocity of large drops and bubbles in media of infinite or restricted extent, *AIChE J.* 6 (1960) 281–288.
- [18] G. Houghton, P.D. Ritchie, J.A. Thomson, Velocity of rise of air bubbles in sea-water, and their types of motion, *Chem. Engrg. Sci.* 7 (1957) 111–112.
- [19] D. Legendre, J. Magnaudet, The lift force on a spherical bubble in a viscous linear shear flow, *J. Fluid Mech.* 368 (1998) 81–126.
- [20] J.T. Lindt, On the periodic nature of the drag on a rising bubble, *Chem. Engrg. Sci.* 27 (1972) 1775–1781.
- [21] E. Loth, M. Taeb-Rahni, G. Tryggvason, Deformable bubbles in a free shear layer, *Int. J. Multiphase Flow* 23 (5) (1997) 977–1001.
- [22] K. Lunde, R.J. Perkins, Shape oscillations of rising bubbles, *Appl. Sci. Res.* 58 (1998) 387–408.
- [23] D. Lörst ad, Numerical modeling of deforming bubble transport related to cavitating hydraulic turbines, PhD Thesis, Department of Heat and Power Engineering, Lund University, 2003. Free download at: <http://www.fm.vok.lth.se/>.
- [24] D. Lörst ad, M. Francois, W. Shyy, L. Fuchs, Assessment of Volume of Fluid and immersed boundary methods for droplet calculations, *Int. J. Numer. Methods Fluids* to be published, 2004.
- [25] J. Magnaudet, I. Eames, The motion of high-Reynolds-number bubbles in inhomogeneous flows, *Annu. Rev. Fluid Mech.* 32 (2000) 659–708.
- [26] W.W. Martin, G.M. Chandler, The local measurement of size and velocity of bubbles rising in liquids, *Appl. Sci. Res.* 38 (1982) 239–246.
- [27] J.B. McLaughlin, Numerical simulation of bubble motion in water, *J. Colloid Interf. Sci.* 184 (1996) 614–625.
- [28] S. Mortazavi, G. Tryggvason, A numerical study of the motion of drops in Poiseuille flow. Part 1. Lateral migration of one drop, *J. Comput. Phys.* 411 (2000) 325–350.
- [29] G. Mougin, J. Magnaudet, Path instability of a rising bubble, *Phys. Rev. Lett.* 88 (1) (2002) 1–4.
- [30] C. Norberg, Fluctuating lift on a circular cylinder: review and new measurements, *J. Fluids and Structures* 17 (2003) 57–96.

- [31] S. Osher, R.P. Fedkiw, Level set methods: an overview and some recent results, *J. Comput. Phys.* 169 (2001) 463–502.
- [32] R.L. Panton, *Incompressible Flow*, Wiley, New York, 1996.
- [33] E.G. Puckett, A.S. Almgren, J.B. Bell, D.L. Marcus, W.J. Rider, A high-order projection method for tracking fluid interfaces in variable density incompressible flows, *J. Comput. Phys.* 130 (1997) 269–282.
- [34] Y. Renardy, M. Renardy, PROST: a parabolic reconstruction of surface tension for the Volume of Fluid method, *J. Comput. Phys.* 183 (2002) 400–421.
- [35] W.J. Rider, D.B. Kothe, Reconstructing volume tracking, *J. Comput. Phys.* 141 (1998) 112–152.
- [36] M. Rudman, Volume-tracking methods for interfacial flow calculations, *Int. J. Numer. Methods Fluids* 24 (1997) 671–691.
- [37] M. Rudman, A volume-tracking method for incompressible multifluid flows with large density variations, *Int. J. Numer. Methods Fluids* 28 (1998) 357–378.
- [38] G. Ryskin, L.G. Leal, Numerical solution of free-boundary problems in fluid mechanics. Part 1 and 2, *J. Fluid Mech.* 148 (1984) 1–35.
- [39] P.G. Saffman, On the rise of small air bubbles in water, *J. Fluid Mech.* 1 (1956) 249–275.
- [40] R. Scardovelli, S. Zaleski, Direct numerical simulation of free-surface and interfacial flow, *Annu. Rev. Fluid Mech* 31 (1999) 567–603.
- [41] S. Shin, D. Juric, Modeling three-dimensional multiphase flow using a level contour reconstruction method for front tracking without connectivity, *J. Comput. Phys.* 180 (2002) 427–470.
- [42] M. Sussman, P. Smereka, S. Osher, A level set approach for computing solutions to incompressible two-phase flow, *J. Comput. Phys.* 114 (1994) 146–159.
- [43] M. Sussman, A.S. Almgren, J.B. Bell, P. Colella, L.H. Howell, M.L. Welcome, An adaptive level set approach for incompressible two-phase flows, *J. Comput. Phys.* 148 (1999) 81–124.
- [44] M. Sussman, E.G. Puckett, A coupled level set and Volume of Fluid method for computing 3D and axisymmetric incompressible two-phase flow, *J. Comput. Phys.* 162 (2000) 301–337.
- [45] S. Takagi, Y. Matsumoto, H. Huang, Numerical analysis of a single rising bubble using boundary-fitted coordinate system, *JSME Int. J. Ser. B* 40 (1) (1997) 42–50.
- [46] A. Tomiyama, A. Sou, H. Minagawa, T. Sakaguchi, Numerical analysis of a single bubble by VOF method, *JSME Int. J. Ser. B* 36 (1) (1993) 51–56.
- [47] A. Tomiyama, G.P. Celata, S. Hosokawa, S. Yoshida, Terminal velocity of single bubbles in surface tension force dominant regime, *Int. J. Multiphase Flow* 28 (2002) 1497–1519.
- [48] G. Tryggvason, B. Bunner, A. Esmaeeli, D. Juric, N. Al-Rawahi, W. Tauber, J. Han, S. Nas, Y.-J. Jan, A front-tracking method for the computations of multiphase flow, *J. Comput. Phys.* 169 (2001) 708–759.
- [49] S.O. Univerdi, G. Tryggvason, A front-tracking method for viscous, incompressible, multi-fluid flows, *J. Comput. Phys.* 100 (1992) 25–37.
- [50] T. Watanabe, K. Ebihara, Numerical simulation of coalescence and breakup of rising droplets, *Comput. Fluids* 32 (2003) 823–834.
- [51] C. Ybert, J.-M. di Meglio, Ascending air bubbles in protein solutions, *Eur. Phys. J. B* 4 (1998) 313–319.
- [52] T. Ye, W. Shyy, J.N. Chung, A fixed-grid, sharp-interface method for bubble dynamics and phase change, *J. Comput. Phys.* 174 (2001) 781–815.
- [53] D.L. Youngs, Time-dependent multi-material flow with large fluid distortion, in: K.W. Morton, M.J. Baines (Eds.), *Numerical Methods for Fluid Dynamics*, Academic Press, New York, 1982, pp. 273–285.
- [54] Y. Zhang, J.A. Finch, A note on single bubble motion in surfactant solutions, *J. Fluid Mech.* 429 (2001) 63–66.